CrossMark

Analysis of Nuclear Structure Properties and Stellar β-decay Rates of Even–Even $^{106–120}$Zr Isotopes

Abdul Kabir[1], Jameel-Un Nabi[2], Syeda Anmol Rida[2], Izzah Anwaar[1], Noor-Ul Ain Raza[1], and Hamad Almujibah[3]

[1] Department of Space Science, Institute of Space Technology, Islamabad 44000, Pakistan; kabirkhanak1@gmail.com
[2] University of Wah, Quaid Avenue, Wah Cantt 47040, Pakistan
[3] Department of Civil Engineering, College of Engineering, Taif University, P.O. Box 11099, Taif 21974, Saudi Arabia

Abstract

The nuclear ground state properties of even–even $^{106–120}$Zr nuclei have been investigated within the framework of the relativistic mean field (RMF) approach. The RMF model with density-dependent DDME2 and DDPC1 interactions is utilized for the calculation of potential energy curves, the nuclear ground-state deformation parameters (β_2), neutron separation energies (S_n and S_{2n}) and neutron skin thickness (r_{np}) of selected Zr isotopes. Later, the β-decay properties of Zr isotopes were studied using the proton-neutron quasi-particle random phase approximation (pn-QRPA) model. These include Gamow–Teller strength distributions, β-decay half-lives and stellar electron emission/positron capture rates. The β_2 values computed from the RMF model were employed in the pn-QRPA model as an input parameter for the calculations of β-decay properties for even–even $^{106–120}$Zr nuclei. The stellar rates were computed using the pn-QRPA framework with three different types of deformation parameters. Only at high temperature ($T_9 \geqslant 2$) and low density ($\rho\, Y_e \leqslant 10^7\, \mathrm{g\, cm}^{-3}$) values, the sum of electron emission and positron capture rates has a sizeable contribution (with positive exponents) to the stellar rates.

Key words: astroparticle physics – elementary particles – nuclear reactions – nucleosynthesis – abundances – (stars:) supernovae: individual (r-process)

1. Introduction

The rapid neutron capture process (*r*-process) is the primary nucleosynthesis mechanism responsible for the production of nuclei more massive than iron (Burbidge et al. 1957). Though the astrophysical regions of this process are contested, it happens in environments with exceptionally high neutron density. The nucleosynthesis route involves neutron-rich isotopes that are far away from the β-stability valley. Important nuclear characteristics (Cowan et al. 1991) for describing the *r*-process are the nuclear masses and beta-decay properties, specifically the β-decay half-lives ($T_{1/2}$) and the β-delayed neutron-emission probabilities (P_n). The β-decay half-life is an observable physical quantity for rare-isotope beam facilities. It determines the timescale of the *r*-process nucleosynthesis. Short half-lives observed at the $A = 110$ mass region enhance the flow of *r*-matter. Neutron-rich nuclei in the mass range of $A \sim 110–120$ have attracted substantial attention from both theoretical and experimental aspects. They are fascinating for many different reasons. For example, they exhibit rapid structural variations in their ground state and low-lying excited states (Wood et al. 1992). At $Z = 40$, the shell structures show a wide range of forms; spherical, prolate, oblate, and other rare tetrahedral shapes (Skalski et al. 1997). Therefore, variations in shape and maximal deformation at deformed subshell closures are to be expected at $Z = 40$. Both relativistic (Xiang et al. 2012) and nonrelativistic (Bender et al. 2008) analysis of structural

evolution for $Z = 40$ and $A \sim 110–120$ indicate the rapid variation of nuclear shapes as varying the nucleon numbers. Shape coexistence is observed, with nuclei exhibiting competing spherical, axially symmetric prolate and oblate, as well as triaxial morphologies at energies close to each other.

Investigating the nuclear masses and charge-changing transition rates of neutron-rich species at radioactive ion-beam facilities has been a major focus in the past decades (Sumikama et al. 2011). However, many exotic nuclear species cannot be studied in terrestrial laboratories, and addressing this issue is best accomplished through theoretical approaches. In neutron-rich environments, electron neutrino captures significantly amplify the effects of β-decays. Moreover, the subsequent neutrino-induced neutron spallation profoundly alters the *r*-abundance distribution pattern (McLaughlin & Fuller 1997). In neutron-rich Zr and Mo isotopes, deformation is a common characteristic. This deformation significantly influences β-decay rates and double β-decay matrix elements in neutron-rich nuclei (Sarriguren et al. 2003). Therefore, it is crucial for theoretical calculations to incorporate these nuclear deformations (Ni & Ren 2014). Sumikama et al. (2011) investigated the low-lying states in ^{106}Zr and ^{108}Zr. They investigated the isomers of $T_{1/2} = 620 \pm 150$ in ^{108}Zr. Furthermore, they discussed different shaped isomers for ^{108}Zr. Kumar et al. (2014) studied the ground/excited state properties for $Z = 40$ isotopes employing the relativistic/non-relativistic mean field

(RMF) approach. They predicted the spherical shape for most of the Zr isotopes in their ground states, and the large deformed one in the low-lying excited states. Nomura et al. (2016) demonstrated rapid structural changes between neutron numbers $N = 58$ and $N = 60$ in isotopes ranging from ^{94}Zr to ^{110}Zr, using the SCMF-to-IBM mapping procedure with the Gogny-D1M effective density functional. Furthermore, β-decay properties also aid in understanding isotopic abundances and potential r-process pathways. Pereira et al. (2009) measured the β-decay properties of certain neutron-rich isotopes ($A \leqslant 110$) including Zr. Sarriguren & Pereira (2010) analyzed the Gamow–Teller (GT) strength distributions, and β-decay properties of neutron-rich nuclei including Zr within the framework of deformed quasi-particle random-phase approximation (QRPA). Yoshida et al. (2023) investigated the β-decay half-lives in the Zr isotopes with shape changes. The GT strength distributions were evaluated in the proton-neutron QRPA and quasiparticle–vibration coupling models. The main purpose of their analysis was to investigate the effect of shape transition over the half-lives.

From the existing literature, we have reached the point that no one has worked on the stellar weak interactions rates for $Z = 40$ within $A = 110-112$. For the analysis of stellar rates we utilize both the RMF (Walecka 1974) and pn-QRPA models to provide a reliable description of the nuclear structure and β-decay properties for these isotopes.

The pn-QRPA theory is capable of performing a microscopic calculation of weak rates for any heavy nuclides. Klapdor et al. (1984) were the first to conduct calculation of β-decay rates for many nuclei far-off from the line of stability using a microscopic nuclear theory. This model was later utilized to calculate the β-decay half-lives of $\sim$6000 neutron-rich nuclei, covering a broad range from the neutron drip line to the line of stability (Staudt et al. 1999). The same pn-QRPA model, with a separable and schematic interaction, was used to perform a microscopic calculation of β^+ electron capture rates of neutron-deficient nuclei with atomic numbers ranging from Zr nuclei of $A \sim 106$–120, extending up to the proton drip line for over 2000 nuclei (Hirsch et al. 1993). The weak interaction rates have contributed significantly to our understanding of the r-process. The instability effects were studied in dense electron-positron-ion plasmas (Usman & Mushtaq 2023). Fuller et al. (1982) conducted a thorough effort to compile these rates at stellar temperatures and densities, with a specific emphasis on decays from excited states of parent nuclei. The pn-QRPA model is extensively employed for its robust and precise computation of β-decay properties in unstable nuclei, under both terrestrial and stellar conditions. Spanning a remarkable range of roughly 6000 nuclei between the neutron drip line and the stability line, the β-decay characteristics have been meticulously investigated using the pn-QRPA framework. This model, employing a schematic and separable interaction, has been applied under both terrestrial (Hirsch et al. 1993) and stellar conditions (Nabi & Klapdor-Kleingrothaus 1999). The pn-QRPA

technique was harnessed to unravel the β-decay properties of waiting point nuclei, focusing on their relevance for astrophysical applications (Nabi et al. 2019). Recent studies have explored the dependence of GT strength on nuclear deformation in neutron-deficient isotopes of $^{178-192}$Hg, $^{185-194}$Pb, $^{67-80}$As (Nabi et al. 2024) and $^{196-206}$Po (Nabi et al. 2023). In this study, we concentrate on neutron-rich nuclei with masses around $A \sim 106$–120, which are highly significant for the astrophysical r-process. Additionally, neutron-rich isotopes within $A \sim 106$–120 are recognized as intriguing examples where the equilibrium shape of the nucleus undergoes rapid changes, and shape coexistence occurs with competing prolate, oblate, and spherical shapes at energies that are closely spaced.

This work is organized as follows: in Section 2, we provide a brief explanation of our models including the RMF and pn-QRPA framework. Section 3 presents the findings and comments. Section 4 contains a summary and conclusions.

2. Theoretical Framework

2.1. The RMF Model

The RMF model depicts nuclei in such a fashion that nucleons interact with each other by exchanging various mesons and photons (Walecka 1974). The initial RMF model had several issues in expressing nuclear surface features and the incompressibility. For this purpose, a nonlinear variant of the model was developed by Ring (1996). Further versions of the model, such as density-dependent (DD) meson exchange (ME) and point coupling (PC), were added, and the concept was referred to as covariant density functional theory (Meng et al. 2006). In this study, we utilized both the DDME and DDPC versions of the model. The DDPC version of the RMF model uses the isoscalar scalar (σ) meson, the isoscalar vector (ω) meson, and the isovector vector (ρ) meson fields to describe nuclear matter and single-particle nuclear characteristics. The DDPC variant of the RMF framework begins with a Lagrangian density (LD) that is given by

$$
\begin{aligned}
\mathcal{L} = {} & \bar{\psi}(i\gamma.\partial - m)\psi \\
& - \tfrac{1}{2}\alpha_S(\hat{\rho})(\bar{\psi}\psi)(\bar{\psi}\psi) - \tfrac{1}{2}\alpha_V(\hat{\rho})(\bar{\psi}\gamma^\mu\psi) \\
& \times (\bar{\psi}\gamma_\mu\psi) - \tfrac{1}{2}\alpha_{TV}(\hat{\rho})(\bar{\psi}\vec{\tau}\gamma^\mu\psi)(\bar{\psi}\vec{\tau}\gamma_\mu\psi) - \tfrac{1}{2}\delta_S(\partial_\nu\bar{\psi}\psi) \\
& \times (\partial^\nu\bar{\psi}\psi) - e\bar{\psi}.A\frac{(1-\tau_3)}{2}\psi.
\end{aligned}
$$

$$(1)$$

Here, the coupling of the protons to the electromagnetic field, the PC interaction terms, and the free-nucleon Lagrangian are the terms covered by Equation (1). The single-nucleon Dirac equation with nucleon self-energies may be produced by varying the Lagrangian with respect to $\bar{\psi}$. For further discussion one can refer to Nikšić et al. (2008).

We employed the DIRHB code (Nikšić et al. 2014) to construct the PECs, β_2, S_n, S_{2n} and r_{np} of $^{106-120}$Zr as a function

of β_2 employing both DDME (Lalazissis et al. 2005) and DDPC interactions. To achieve this, RMF calculations with quadrupole moment constraints were carried out. For open-shell nuclei, pairing correlations are crucial, and the BCS approximation was employed to address these correlations. Moreover, all the above mentioned ground state computations were performed utilizing the constant G approximation (Karatzikos et al. 2010).

2.2. The pn-QRPA Model

This section discusses the formalism used to calculate the beta decay properties including the stellar weak rates at all temperatures and all densities, which are relevant to stellar environments, using the pn-QRPA theory. The pn-QRPA framework was used to compute the GT strength and the terrestrial β-decay half-lives. The Hamiltonian in the pn-QRPA model is structured as follows

$$\mathfrak{H}^{\mathrm{QRPA}} = \mathfrak{H}^{\mathrm{sp}} + \mathscr{V}^{\mathrm{pair}} + \mathscr{V}^{\mathrm{pp}}_{\mathrm{GT}} + \mathscr{V}^{\mathrm{ph}}_{\mathrm{GT}}, \qquad (2)$$

where $\mathfrak{H}^{\mathrm{sp}}$ denotes the single-particle Hamiltonian, and $\mathscr{V}^{\mathrm{pair}}$ represents the nucleon–nucleon pairing interaction. $\mathscr{V}^{\mathrm{pp}}_{\mathrm{GT}}$ is the particle–particle (pp) and $\mathscr{V}^{\mathrm{ph}}_{\mathrm{GT}}$ is particle-hole (ph) GT forces. The Nilsson model was utilized to assess the single-particle's wave functions and energies (Nilsson 1955). The oscillator constant is analyzed employing: $\hbar\omega = (45A^{-1/3} - 25A^{-2/3})$. The Nilsson-potential variables were selected based on Ragnarsson & Sheline (1984). The values of mass excess were taken from AME2020 (Wang et al. 2021) for the analysis of Q-values. We used β_2 values that were adopted from Möller et al. (2016) and RMF based analysis.

The pairing force was calculated using the BCS approximation. These calculations were performed separately for both proton and neutron. We took a constant pairing force of strength G (G_p and G_n for protons and neutrons, respectively),

$$\mathscr{V}_{\mathrm{pair}} = -G \sum_{jkj'k'} (-1)^{l+j-k} s^{\dagger}_{jk} s^{\dagger}_{j-k}$$
$$\times (-1)^{l'+j'-k'} s_{j'-k'} s_{j'k'}, \qquad (3)$$

where l represents the orbital angular momentum and the summation over k and k' is constrained to positive values. $(s^{\dagger}_{jk}, s_{jk})$, the spherical nucleon basis, was transformed into a deformed basis $(d^{\dagger}_{k\alpha}, d_{k\alpha})$, using the following equation

$$d^{\dagger}_{k\alpha} = \Sigma_j \mathbb{D}^{k\alpha}_j s^{\dagger}_{jk}. \qquad (4)$$

The matrices $\mathbb{D}^{k\alpha}$ were obtained by diagonalizing the Nilsson Hamiltonian, and α represents the additional quantum numbers. The quasiparticle basis $(q^{\dagger}_{k\alpha}, q_{k\alpha})$ was introduced using the Bogoliubov transformation

$$q^{\dagger}_{k\alpha} = u_{k\alpha} d^{\dagger}_{k\alpha} - v_{k\alpha} d_{\bar{k}\alpha}, \qquad (5)$$

$$q^{\dagger}_{\bar{k}\alpha} = u_{k\alpha} d^{\dagger}_{\bar{k}\alpha} + v_{k\alpha} d_{k\alpha}, \qquad (6)$$

where the time-reversed state of k was expressed by $\bar{k}$. The occupancy amplitudes met the basis $v^2_{k\alpha} + u^2_{k\alpha} = 1$ and were determined using the BCS equations. Ground-state correlation is introduced by adding a residual interaction to the Hamiltonian, which is then treated within the RPA framework. The creation operators of QRPA phonons are defined as follows

$$A^{\dagger}_{\omega}(\mu) = \sum_{pn} [X^{pn}_{\omega}(\mu) q^{\dagger}_p q^{\dagger}_{\bar{n}} - Y^{pn}_{\omega}(\mu) q_n q_{\bar{p}}], \qquad (7)$$

where p (proton) and n (neutron) indices are the quasiparticle states. The summation was over p–n pairs satisfying the conditions: $\mu = k_p - k_n = (-1, 0, 1)$ and $\pi_p.\pi_n = 1$. The amplitudes of the pn-QRPA phonon are (X_{ω}, Y_{ω}) and the RPA equation's eigenvalue is expressed by the excitation energy ω. The pp (κ) and ph (χ) are GT forces known as residual interactions in the pn-QRPA model. The pp interaction was incorporated in our Hamiltonian using

$$\mathscr{V}^{\mathrm{pp}}_{\mathrm{GT}} = -2\kappa \sum_{\mu=-1}^{1} (-1)^{\mu} \mathcal{O}^{\dagger}_{\mu} \mathcal{O}_{-\mu}, \qquad (8)$$

with

$$\mathcal{O}^{\dagger}_{\mu} = \sum_{j_p k_p j_n k_n} \langle j_n k_n | (t_{\pm} \sigma_{\mu})^{\dagger} | j_p k_p \rangle$$
$$\times (-1)^{l_n + j_n - k_n} s^{\dagger}_{j_p k_p} s^{\dagger}_{j_n - k_n}. \qquad (9)$$

Similarly, for the analysis of ph interaction, we employed

$$\mathscr{V}^{\mathrm{ph}}_{\mathrm{GT}} = +2\chi \sum_{\mu=-1}^{1} (-1)^{\mu} \mathcal{U}_{\mu} \mathcal{U}^{\dagger}_{-\mu}, \qquad (10)$$

with

$$\mathcal{U}_{\mu} = \sum_{j_p k_p j_n k_n} < j_p k_p | t_{\pm} \sigma_{\mu} | j_n k_n > s^{\dagger}_{j_p k_p} s_{j_n k_n}. \qquad (11)$$

The inclusion of the GT residual interaction significantly alters the calculated GT strength distribution and is crucial for accurately reproducing the observed GT strength functions. The pp and ph GT residual strengths were calculated using the ratios $0.58/A^{0.7}$ and $5.2/A^{0.7}$, respectively (Homma et al. 1996). Our findings supported the model-independent Ikeda sum rule (Ikeda et al. 1963). The GT transition probabilities have been determined utilizing

$$B_{\mathrm{GT}}(\omega) = |\langle \omega, \mu || \tau_{\pm} \sigma_{\mu} || \mathrm{QRPA} \rangle|^2. \qquad (12)$$

The partial half-lives $t_{1/2}$ were determined employing the equation

$$t_{1/2} = \frac{K}{(g_A/g_V)^2 f_A(A, Z, E) B_{\mathrm{GT}}(\omega) + f_V(A, Z, E) B_{\mathrm{F}}(\omega)}, \qquad (13)$$

where $K = 6143$ s (Hardy & Towner 2009). The ratio g_A/g_V was taken as -1.2694 (Nakamura & Particle Data Group 2010).

$f_V(A, Z, E)$ (vector transition) and $f_A(A, Z, E)$ (axial vector transition) are the phase space integrals, B_{GT} is the GT transition probabilities, and B_F is the Fermi transition probabilities. Analysis of B_F is quite easy and may be observed from Hirsch et al. (1991). The terrestrial half-lives of β-decay were computed as

$$T_{1/2} = \left(\sum_{0 \leqslant \omega \leqslant Q} (\frac{1}{t_{1/2}}) \right)^{-1}. \tag{14}$$

For further analysis of Equation (2), one can refer to Staudt et al. (1999).

The stellar β-decay (we subsequently refer to this as electron emission, EE) and positron capture (PC) rates between parent level n and daughter state m have been determined utilizing

$$\lambda_{mn}^{EE/PC} = \ln 2 \frac{f_{mn}^{EE/PC}(\rho, T, E_f)}{(ft)_{mn}}, \tag{15}$$

where $(ft)_{mn}$ corresponds to the GT and Fermi transitions

$$B^{mn} = (g_A/g_V)^2 B_{GT}^{mn} + B_F^{mn}, \tag{16}$$

$$B_{GT}^{mn} = \frac{1}{2J_m + 1} \langle n \| \sum_k \tau_\pm^k \vec{\sigma}^k \| m \rangle |^2, \tag{17}$$

$$B_F^{mn} = \frac{1}{2J_m + 1} \langle n \| \sum_k \tau_\pm^k \| m \rangle |^2. \tag{18}$$

The construction of low-lying excited levels and computation of nuclear matrix elements in our present analysis may be found in Muto et al. (1992). f_{mn} is the phase space and depends on the core temperature (T), core density (ρ) and Fermi energy (E_f). It was calculated using the equation

$$f_{mn}^{EE} = \int_1^{E_\beta} E_k \sqrt{E_k^2 - 1} (E_\beta - E_k)^2 F(+Z, E_k)$$
$$\times (1 - \mathcal{R}_-) dE_k, \tag{19}$$

for EE decay rates. The f_{nm} for PC were computed using the relation

$$f_{mn}^{PC} = \int_{E_l}^{\infty} E_k \sqrt{E_k^2 - 1} (E_\beta + E_k)^2 F(-Z, E_k) \mathcal{R}_+ dE_k, \tag{20}$$

where E_k is the kinetic energy of electron and E_l is the total capture threshold energy. The Fermi functions, $F(\pm Z, E_k)$, were calculated using the method described in Gove & Martin (1971). The total β decay energy was determined using

$$E_\beta = m_p - m_d + E_m - E_n, \tag{21}$$

where E_n is the excitation energy of the daughter nucleus having mass m_d while E_m is the corresponding quantity of parent nucleus with mass m_p. The distribution functions have been determined with

$$\mathcal{R}_- = \left[\exp\left(\frac{E_k - E_f}{k_\beta T} \right) + 1 \right]^{-1}, \tag{22}$$

$$\mathcal{R}_+ = \left[\exp\left(\frac{E_k + 2 - E_f}{k_\beta T} \right) + 1 \right]^{-1}, \tag{23}$$

where k_β is the Boltzmann constant. The electron number density, related to nuclei and protons, is determined using the relationship

$$\rho Y_e N_A = \frac{1}{\pi^2} \left(\frac{m_e c}{\hbar} \right)^3 \int_0^\infty (\mathcal{R}_- - \mathcal{R}_+) p^2 dp, \tag{24}$$

here N_A represents the Avogadro number, Y_e is for the ratio of electron number to baryon number and p represents the momentum of positron/electron. The total stellar weak rates are computed using

$$\lambda^{EE/PC} = \sum_{mn} P_m \lambda_{mn}^{EE/PC}, \tag{25}$$

where P_m, which is calculated using the Boltzmann distribution, is the occupancy probability of the parent excited states. We continue to sum the initial and final states until our rate computation reaches the necessary degree of convergence.

3. Result and Discussions

We have provided the detailed calculations of the binding energy, one- and two-neutron separation energies, neutron skin thickness (r_{np}), and nuclear deformation (β_2) for $^{106-120}$Zr isotopes using the RMF DDME2 and DDPC1 functionals. We have investigated β_2 for $^{106-120}$Zr nuclei in depth. To accomplish this, we performed PEC calculations of the chosen nuclei within the RMF framework. We implemented constraints on the quadrupole moment to compute the binding energy for the analysis of PECs. The PECs were obtained by calculating the difference between the binding energy for specific β_2 values and the lowest binding energy for the nuclei under investigation. Nuclear shapes were determined by the PEC minima. Prolate nuclei resulted from a PEC minimum located on the positive side of β_2, whereas oblate nuclei were found on the negative side of β_2. Figure 1 shows the potential energy curves for even–even $^{106-120}$Zr isotopes, plotted as a function of β_2. The PECs obtained from RMF calculations for even–even isotopes $^{106-120}$Zr show that both DDME2 and DDPC1 exhibit well-developed oblate and spherical shapes at the energy minima. The transitions occur from oblate to spherical shapes for $^{106-108}$Zr. For example, the ground states of $^{106-116}$Zr are located in the oblate sector with $\beta_2 = -0.36$ for DDPC1 interactions. Similarly, DDME2 gives an oblate morphology for $^{106-108}$Zr and a prolate minimum for ^{110}Zr. In the isotopic region $^{112-120}$Zr via DDME2 and $^{118-120}$Zr via DDPC1, spherical shapes are exhibited. The general trend observed is the gradual disappearance of both prolate and oblate minima, collapsing into spherical shapes in the heavier
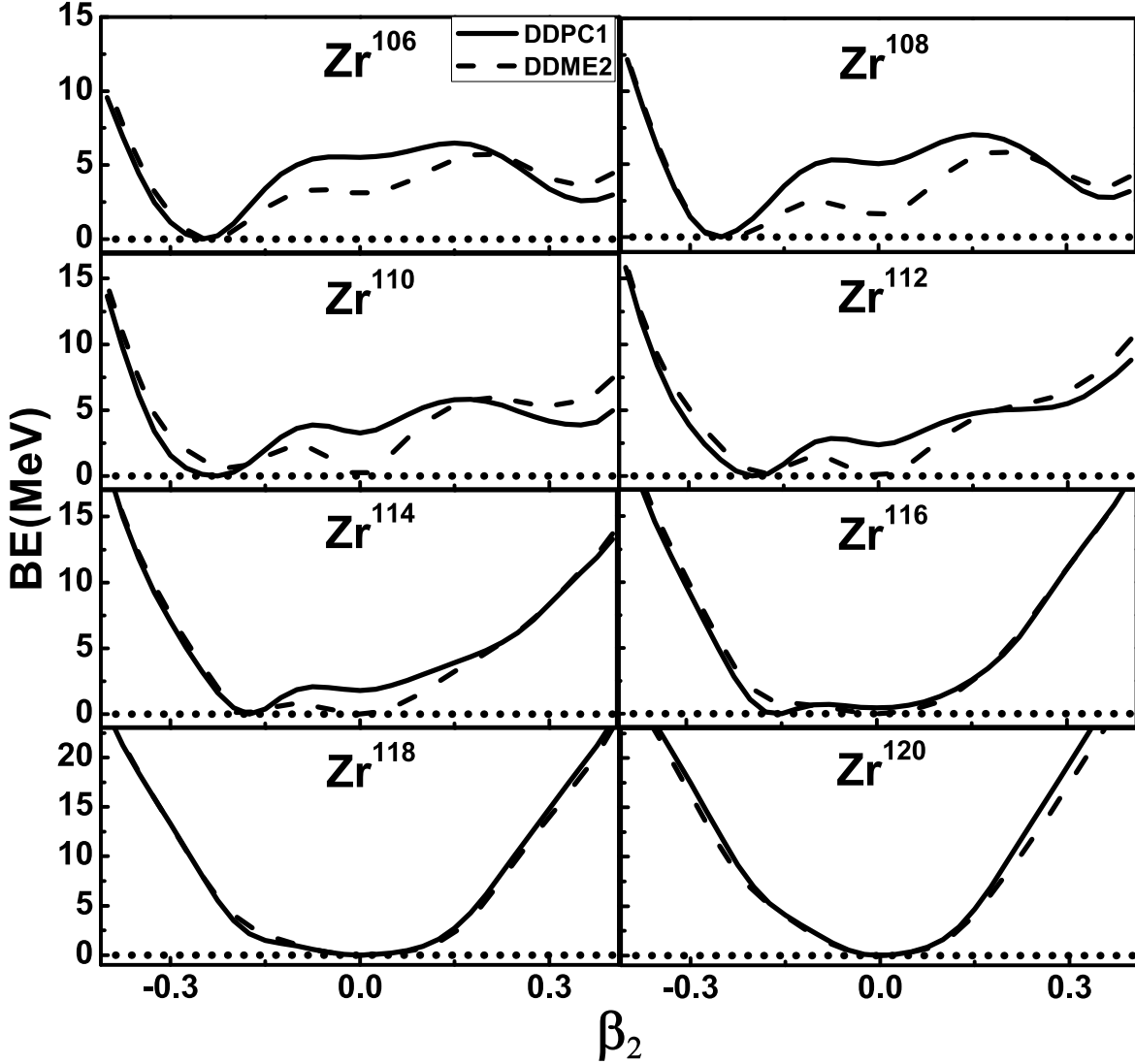
Figure 1. Potential energy curves for even–even $^{106-120}$Zr isotopes obtained from DDME2 and DDPC1 functionals.

isotopes at the magic number $N = 82$. The present computed β_2 values, along with those from Möller et al. (2016), are displayed in Table 1. Neutron separation energies for one-neutron (S_n) and two-neutron (S_{2n}) are defined as:

$$S_n(Z, N) = E_b(Z, N) - E_b(Z, N - 1), \qquad (26)$$

$$S_{2n}(Z, N) = E_b(Z, N) - E_b(Z, N - 2), \qquad (27)$$

where $E_b(Z, N)$, $E_b(Z, N - 1)$, and $E_b(Z, N - 2)$ are the binding energies for the Zr nuclei, obtained by employing the RMF model with DDME2 and DDPC1 interactions. S_n indicates the stability of a nucleus against the emission of a single neutron. A higher S_n value means the nucleus is more stable and less likely to lose a neutron, whereas S_{2n} provides information on the stability of a nucleus against the emission of two neutrons. This

is particularly important for defining the neutron drip lines, which mark the limits where neutron-rich isotopes can exist. Generally, S_{2n} decreases with an increasing number of neutrons, indicating reduced stability as more neutrons are added. However, a sharp change in the S_{2n} slope is observed at magic numbers due to neutron shell closures, which confer extra stability to the nucleus. This is illustrated in Figures 2 and 3. The FRDM-based computed results for S_n are close to the experimental data, while the S_n computed via the RMF DDPC1-based interaction is, on average, 0.45 MeV lower than the measured data. However, the computed S_{2n} values are in good agreement with both the FRDM calculations and experimental data (Wang et al. 2021). Investigating magic shell nuclei is important for understanding the r-process
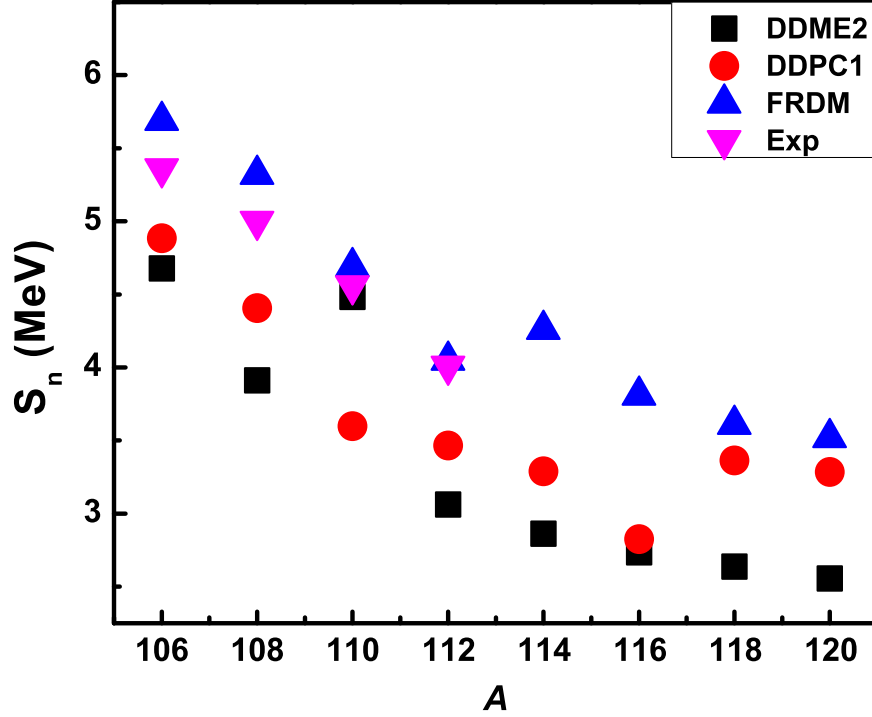
Figure 2. The S_n for $^{106-120}$Zr using the RMF with DDME2 and DDPC1 interactions along with the experimental data and FRDM (Möller et al. 2016) based results.

Table 1
β_2 Values adopted from the FRDM (Möller et al. 2016) and those Computed Using the RMF Framework with DDME2 and DDPC1 Interactions

Nuclei	FRDM	DDME2	DDPC1
^{106}Zr	0.368	−0.403	−0.447
^{108}Zr	0.358	−0.451	−0.451
^{110}Zr	0.359	0	−0.408
^{112}Zr	0.359	0	−0.364
^{114}Zr	−0.185	0	−0.321
^{116}Zr	−0.164	0	−0.276
^{118}Zr	−0.154	0	0
^{120}Zr	0	0	0

nucleosynthesis. At the magic point level, the S_n shows discontinuities, reducing the neutron capture rates. As a consequence, the r-process matter flow moves closer to stability, where nuclei have substantially larger β-decay half-lives.

Neutron skin thickness $r_{np} = r_n - r_p$ has to be well understood for astrophysics and nuclear physics challenges. As an illustration, the neutron skin thickness and the slope parameter of the symmetry energy of nuclear matter are connected. The r_{np} for the Zr nuclei under our investigation is plotted in Figure 4 along with the DDMEX and DDPCX prediction of Liu et al. (2024). From the basic knowledge of nuclear physics, r_{np} increases linearly with the addition of neutrons in the isotopic channel.

After the analysis of the nuclear ground state properties, we want to focus the reader's attention on the detailed analysis of nuclear structure and stellar beta decay properties, including the GT strength, half-lives, and stellar rates for even–even Zr nuclei. For this purpose, we employed the pn-QRPA model. For the analysis of the beta decay properties, we have tested the deformation parameters. For example, we applied the β_2 to the deformed Nilsson potential as an input for the analysis of the beta decay properties. The β_2 employed in the pn-QRPA from the FRDM is considered as pn-QRPA-FRDM. Similarly, the β_2 employed in the pn-QRPA from the RMF-DDPC1 and RMF-DDME2 is considered as pn-QRPA-DDPC1 and pn-QRPA-DDME2, respectively. The analysis of our present recipe is depicted in Figures 5–7. Figure 5 shows the computed GT strength for ^{106}Zr along with experimental data (Ha et al. 2020). One can observe that the predicted GT strength transitions computed with the FRDM and RMF-based β_2 are in good agreement with the available measured data. Figure 6 shows the computed GT for ^{108}Zr along with experimental data (Ha et al. 2020). The pn-QRPA-FRDM and pn-QRPA-DDPC1 are well matched at lower and higher excitation energies. However, the pn-QRPA-DDME2 intensities are higher than the pn-QRPA-FRDM and pn-QRPA-DDPC1 based predictions. The same trend is found for ^{110}Zr, as depicted in Figure 7. Overall, the predicted GT strength shows good agreement with the measured data (Ha et al. 2020). The pn-QRPA model was used to calculate the β-decay
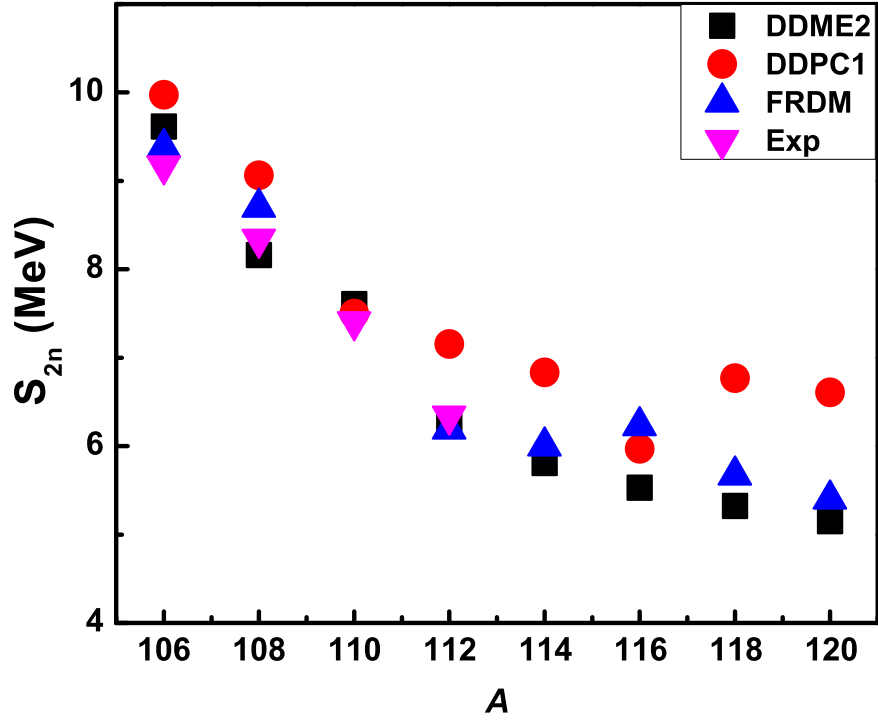
Figure 3. The S_{2n} for $^{106-120}$Zr using the RMF with DDME2 and DDPC1 interactions along with the experimental data (Wang et al. 2021) and FRDM (Möller et al. 2016) based results.
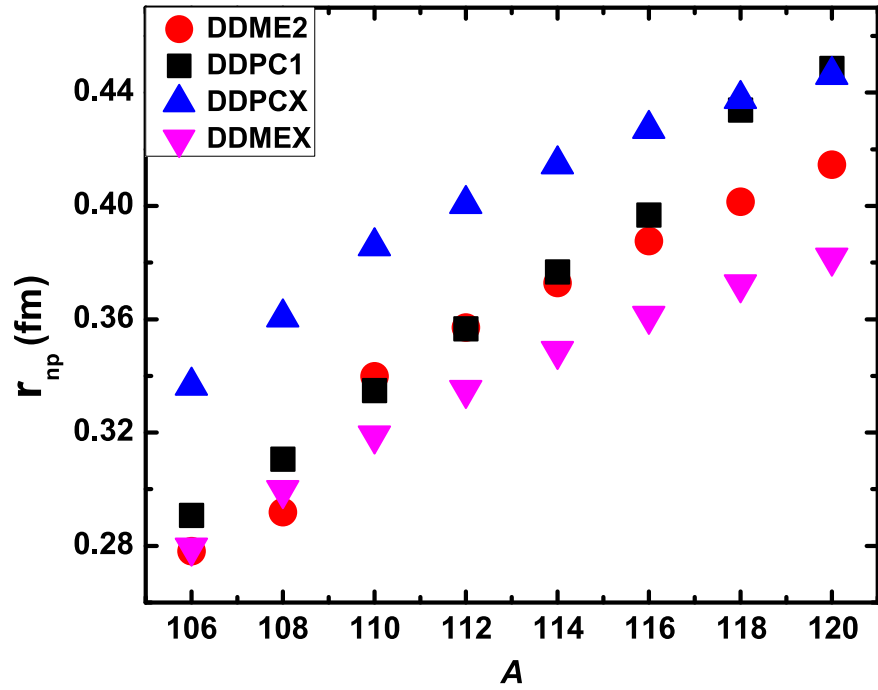
Figure 4. The r_{np} for even–even $^{106-120}$Zr using the RMF with DDME2 and DDPC1 interactions along with the predictions of Liu et al. (2024).
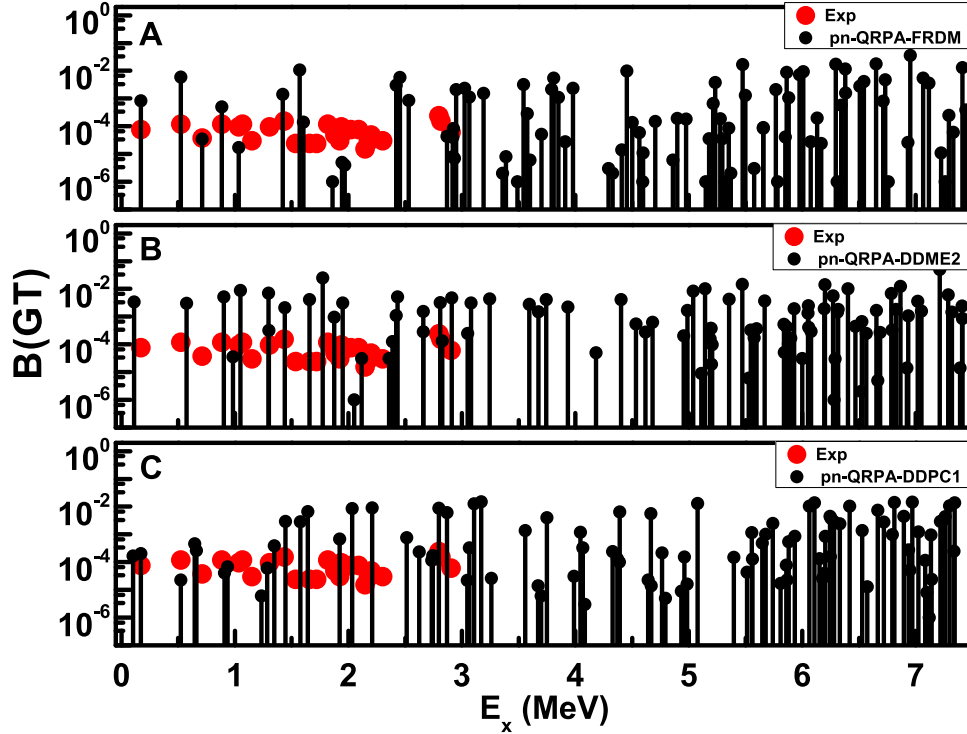
Figure 5. Comparison of the pn-QRPA calculated GT strength distributions for ^{106}Zr with experimental data (Ha et al. 2020). (A) The computed GT strength using the pn-QRPA-FRDM model. (B) The computed GT strength using the pn-QRPA-DDME2 model. (C) The computed GT strength using the pn-QRPA-DDPC1 model.

half-lives of even–even Zr isotopes in the mass region $106 \leqslant A \leqslant 120$. The analysis of the terrestrial half-lives for the Zr isotopes, computed via the pn-QRPA model, along with measured data (Wang et al. 2021), is shown in Figure 8. Remarkably, our calculations via pn-QRPA-FRDM and pn-QRPA-DDPC1 agree with the measured half-lives within a factor of 2 while the same calculations via pn-QRPA-DDME2 align with the measured half-lives within a factor of 1.2. This underscores the robustness of the pn-QRPA model, which is renowned for its predictive accuracy in neutron-rich nuclei. One can see from Figure 8 that the present prediction for half-lives based on the pn-QRPA-DDME2 is more closely fitted with the measured data.

After analyzing the terrestrial half-lives, we examined the stellar PC and EE rates for the Zr nuclei. The residual interaction parameters were optimized based on the terrestrial half-lives and the Ikeda sum rule (where experimental half-lives were not available). We analyzed the stellar rates at densities $\rho Y_e = 10^4$, 10^7 and 10^{10} g cm^{-3} at temperatures $T_9 = 2$–10 (where T_9 is in units of 10^9 K). No explicit quenching factor was included in pn-QRPA calculations. The stellar rates increase with soaring core temperatures. This occurs because the occupation probability of parent excited

states rises with temperature, leading to a finite contribution to the total stellar rates. Increasing the density of the stellar core results in substantial reduction of the available phase space. This in turns leads to smaller rates, see Equation (15) (Kabir et al. 2024). To the best of our knowledge, the stellar rates for $^{106-120}$Zr have not been calculated in the past. We performed the stellar rate calculations using the pn-QRPA model with three different values of deformation parameter as before. The EE and PC rates for ^{106}Zr to ^{120}Zr are listed in Table 2. The $\lambda_{(EE+PC)}^{pn-QRPA-DDME2}$ values are higher than $\lambda_{(EE+PC)}^{pn-QRPA-DDPC1}$ and $\lambda_{(EE+PC)}^{pn-QRPA-FRDM}$. Qualitatively, $\lambda_{(EE+PC)}^{pn-QRPA-DDME2}$ is higher than $\lambda_{(EE+PC)}^{pn-QRPA-DDPC1}$ by a factor of 1.2 at $T_9 = 10$ and $\rho Y_e = 10^4$ g cm^{-3} to 10^{10} g cm^{-3} for ^{106}Zr. Similarly, $\lambda_{(EE+PC)}^{pn-QRPA-DDME2}$ is higher than $\lambda_{(EE+PC)}^{pn-QRPA-FRDM}$ by a factor of 1.85. This trend is similar for the EE and PC rates up to ^{118}Zr.

However, for ^{120}Zr, $\lambda_{(EE+PC)}^{pn-QRPA-DDME2}$ is higher than $\lambda_{(EE+PC)}^{pn-QRPA-DDPC1}$ by a factor of 2.62 at $T_9 = 10$ and $\rho Y_e = 10^4$ g cm^{-3}. At $\rho Y_e = 10^7$ g cm^{-3} and 10^{10} g cm^{-3}, this factor reduces to 1.02. The same factors are observed for the ratio of $\lambda_{(EE+PC)}^{pn-QRPA-DDME2}$ to $\lambda_{(EE+PC)}^{pn-QRPA-FRDM}$. Generally, at low densities and high temperatures the stellar weak rates are meaningful, possessing magnitudes with positive exponents. This can be seen from Table 2.
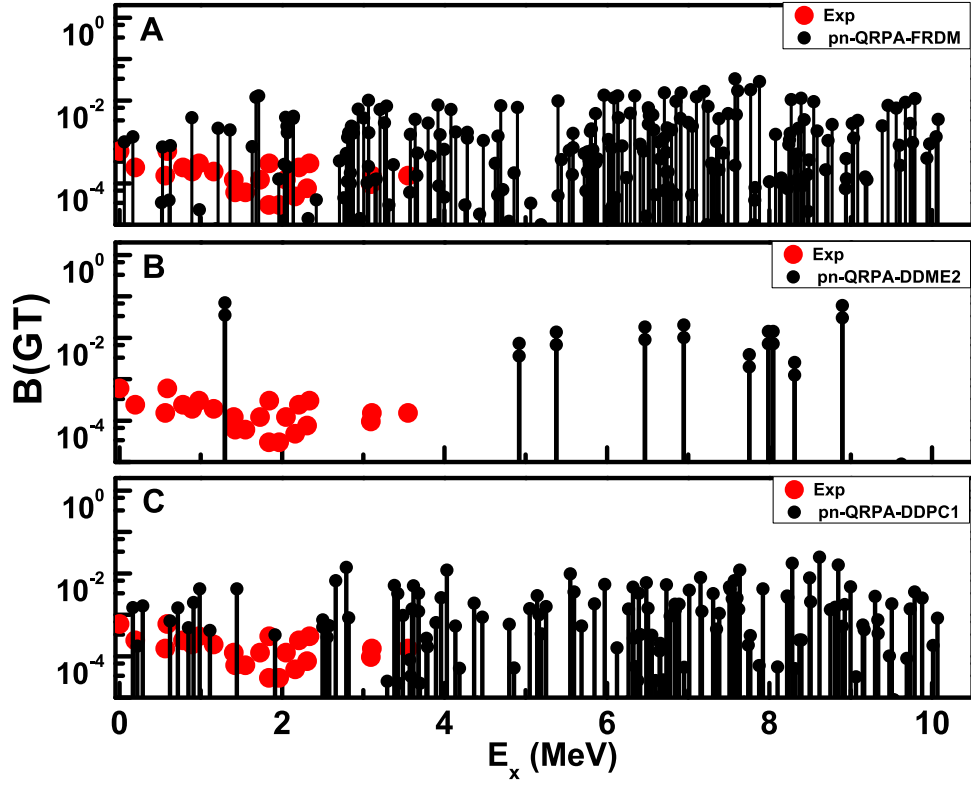
Figure 6. Same as Figure 5 but for ^{108}Zr.
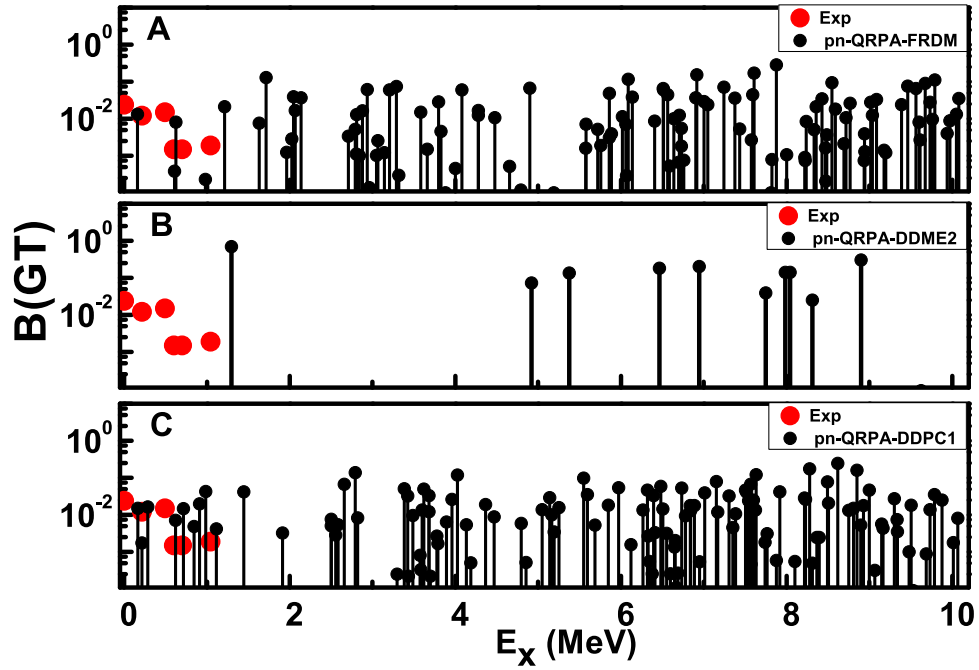
Figure 7. Same as Figure 5 but for ^{110}Zr.

Table 2
Sum of EE and PC Stellar Rates for Zr Isotopes as a Function of Core Temperature (T_9) and Density ($\rho\, Y_e$), Presented in Units of s^{-1} and $\mathrm{g\,cm}^{-3}$, Respectively

| | | ^{106}Zr | | | ^{108}Zr | | | ^{110}Zr | | |
$\rho\, Y_e$	T_9	$\lambda^{\mathrm{pn-QRPA-FRDM}}_{(\mathrm{EE+PC})}$	$\lambda^{\mathrm{pn-QRPA-DDPC1}}_{(\mathrm{EE+PC})}$	$\lambda^{\mathrm{pn-QRPA-DDME2}}_{(\mathrm{EE+PC})}$	$\lambda^{\mathrm{pn-QRPA-FRDM}}_{(\mathrm{EE+PC})}$	$\lambda^{\mathrm{pn-QRPA-DDPC1}}_{(\mathrm{EE+PC})}$	$\lambda^{\mathrm{pn-QRPA-DDME-2}}_{(\mathrm{EE+PC})}$	$\lambda^{\mathrm{pn-QRPA-FRDM}}_{(\mathrm{EE+PC})}$	$\lambda^{\mathrm{pn-QRPA-DDPC1}}_{(\mathrm{EE+PC})}$	$\lambda^{\mathrm{pn-QRPA-DDME2}}_{(\mathrm{EE+PC})}$
	2	$3.64 \times 10^{+00}$	$4.01 \times 10^{+00}$	$8.32 \times 10^{+00}$	$8.69 \times 10^{+00}$	$1.00 \times 10^{+01}$	$1.69 \times 10^{+01}$	$1.93 \times 10^{+01}$	$2.51 \times 10^{+01}$	$6.68 \times 10^{+01}$
	4	$3.70 \times 10^{+00}$	$4.10 \times 10^{+00}$	$8.47 \times 10^{+00}$	$8.84 \times 10^{+00}$	$1.03 \times 10^{+01}$	$1.70 \times 10^{+01}$	$1.94 \times 10^{+01}$	$2.54 \times 10^{+01}$	$7.20 \times 10^{+01}$
10^4	6	$4.31 \times 10^{+00}$	$5.23 \times 10^{+00}$	$9.71 \times 10^{+00}$	$1.04 \times 10^{+01}$	$1.28 \times 10^{+01}$	$1.90 \times 10^{+01}$	$2.14 \times 10^{+01}$	$2.93 \times 10^{+01}$	$1.06 \times 10^{+02}$
	8	$5.78 \times 10^{+00}$	$7.40 \times 10^{+00}$	$1.23 \times 10^{+01}$	$1.40 \times 10^{+01}$	$1.69 \times 10^{+01}$	$2.34 \times 10^{+01}$	$2.67 \times 10^{+01}$	$3.75 \times 10^{+01}$	$1.66 \times 10^{+02}$
	10	$7.53 \times 10^{+00}$	$9.43 \times 10^{+00}$	$1.49 \times 10^{+01}$	$1.82 \times 10^{+01}$	$2.04 \times 10^{+01}$	$2.80 \times 10^{+01}$	$3.34 \times 10^{+01}$	$4.56 \times 10^{+01}$	$2.25 \times 10^{+02}$
	2	$3.45 \times 10^{+00}$	$3.77 \times 10^{+00}$	$7.94 \times 10^{+00}$	$8.34 \times 10^{+00}$	$9.64 \times 10^{+00}$	$1.63 \times 10^{+01}$	$1.87 \times 10^{+01}$	$2.44 \times 10^{+01}$	$6.55 \times 10^{+01}$
	4	$3.55 \times 10^{+00}$	$3.92 \times 10^{+00}$	$8.15 \times 10^{+00}$	$8.57 \times 10^{+00}$	$1.00 \times 10^{+01}$	$1.66 \times 10^{+01}$	$1.90 \times 10^{+01}$	$2.49 \times 10^{+01}$	$7.08 \times 10^{+01}$
10^7	6	$4.19 \times 10^{+00}$	$5.07 \times 10^{+00}$	$9.47 \times 10^{+00}$	$1.02 \times 10^{+01}$	$1.26 \times 10^{+01}$	$1.86 \times 10^{+01}$	$2.10 \times 10^{+01}$	$2.89 \times 10^{+01}$	$1.05 \times 10^{+02}$
	8	$5.64 \times 10^{+00}$	$7.23 \times 10^{+00}$	$1.20 \times 10^{+01}$	$1.37 \times 10^{+01}$	$1.66 \times 10^{+01}$	$2.30 \times 10^{+01}$	$2.63 \times 10^{+01}$	$3.70 \times 10^{+01}$	$1.65 \times 10^{+02}$
	10	$7.37 \times 10^{+00}$	$9.23 \times 10^{+00}$	$1.46 \times 10^{+01}$	$1.78 \times 10^{+01}$	$2.00 \times 10^{+01}$	$2.76 \times 10^{+01}$	$3.30 \times 10^{+01}$	$4.50 \times 10^{+01}$	$2.23 \times 10^{+02}$
	2	2.57×10^{-11}	2.13×10^{-11}	5.89×10^{-11}	9.82×10^{-09}	1.64×10^{-08}	2.60×10^{-08}	8.57×10^{-06}	2.35×10^{-05}	3.21×10^{-05}
	4	3.42×10^{-06}	4.32×10^{-06}	7.29×10^{-06}	5.90×10^{-05}	1.25×10^{-04}	1.52×10^{-04}	1.04×10^{-03}	3.27×10^{-03}	3.13×10^{-02}
10^{10}	6	3.33×10^{-04}	4.89×10^{-04}	6.65×10^{-04}	2.35×10^{-03}	4.57×10^{-03}	5.26×10^{-03}	1.72×10^{-02}	4.46×10^{-02}	4.01×10^{-01}
	8	3.85×10^{-03}	5.42×10^{-03}	7.05×10^{-03}	1.87×10^{-02}	2.90×10^{-02}	3.56×10^{-02}	9.55×10^{-02}	2.00×10^{-01}	$1.60 \times 10^{+00}$
	10	1.72×10^{-02}	2.23×10^{-02}	2.94×10^{-02}	6.86×10^{-02}	8.81×10^{-02}	1.15×10^{-01}	2.81×10^{-01}	5.08×10^{-01}	$3.85 \times 10^{+00}$

| | | ^{112}Zr | | | ^{114}Zr | | | ^{116}Zr | | |
$\rho\, Y_e$	T_9	$\lambda^{\mathrm{pn-QRPA-FRDM}}_{(\mathrm{EE+PC})}$	$\lambda^{\mathrm{pn-QRPA-DDPC1}}_{(\mathrm{EE+PC})}$	$\lambda^{\mathrm{pn-QRPA-DDME-2}}_{(\mathrm{EE+PC})}$	$\lambda^{\mathrm{pn-QRPA-FRDM}}_{(\mathrm{EE+PC})}$	$\lambda^{\mathrm{pn-QRPA-DDPC1}}_{(\mathrm{EE+PC})}$	$\lambda^{\mathrm{pn-QRPA-DDME-2}}_{(\mathrm{EE+PC})}$	$\lambda^{\mathrm{pn-QRPA-FRDM}}_{(\mathrm{EE+PC})}$	$\lambda^{\mathrm{pn-QRPA-DDPC1}}_{(\mathrm{EE+PC})}$	$\lambda^{\mathrm{pn-QRPA-DDME2}}_{(\mathrm{EE+PC})}$
	2	$3.29 \times 10^{+01}$	$3.88 \times 10^{+01}$	$3.53 \times 10^{+01}$	$5.18 \times 10^{+01}$	$3.72 \times 10^{+01}$	$8.30 \times 10^{+01}$	$1.15 \times 10^{+02}$	$6.82 \times 10^{+01}$	$1.84 \times 10^{+02}$
	4	$3.41 \times 10^{+01}$	$4.35 \times 10^{+01}$	$3.64 \times 10^{+01}$	$5.18 \times 10^{+01}$	$3.71 \times 10^{+01}$	$8.30 \times 10^{+01}$	$1.19 \times 10^{+02}$	$7.12 \times 10^{+01}$	$2.04 \times 10^{+02}$
10^4	6	$3.98 \times 10^{+01}$	$5.01 \times 10^{+01}$	$4.33 \times 10^{+01}$	$5.29 \times 10^{+01}$	$3.78 \times 10^{+01}$	$8.49 \times 10^{+01}$	$1.36 \times 10^{+02}$	$8.55 \times 10^{+01}$	$3.01 \times 10^{+02}$
	8	$4.93 \times 10^{+01}$	$5.60 \times 10^{+01}$	$5.45 \times 10^{+01}$	$5.96 \times 10^{+01}$	$4.27 \times 10^{+01}$	$9.50 \times 10^{+01}$	$1.57 \times 10^{+02}$	$1.04 \times 10^{+02}$	$4.41 \times 10^{+02}$
	10	$5.84 \times 10^{+01}$	$6.06 \times 10^{+01}$	$6.49 \times 10^{+01}$	$7.38 \times 10^{+01}$	$5.40 \times 10^{+01}$	$1.16 \times 10^{+02}$	$1.74 \times 10^{+02}$	$1.18 \times 10^{+02}$	$5.65 \times 10^{+02}$
	2	$3.21 \times 10^{+01}$	$3.80 \times 10^{+01}$	$3.45 \times 10^{+01}$	$5.08 \times 10^{+01}$	$3.62 \times 10^{+01}$	$8.17 \times 10^{+01}$	$1.14 \times 10^{+02}$	$6.71 \times 10^{+01}$	$1.82 \times 10^{+02}$
	4	$3.36 \times 10^{+01}$	$4.29 \times 10^{+01}$	$3.57 \times 10^{+01}$	$5.09 \times 10^{+01}$	$3.64 \times 10^{+01}$	$8.18 \times 10^{+01}$	$1.18 \times 10^{+02}$	$7.01 \times 10^{+01}$	$2.02 \times 10^{+02}$
10^7	6	$3.93 \times 10^{+01}$	$4.96 \times 10^{+01}$	$4.27 \times 10^{+01}$	$5.22 \times 10^{+01}$	$3.73 \times 10^{+01}$	$8.40 \times 10^{+01}$	$1.35 \times 10^{+02}$	$8.48 \times 10^{+01}$	$2.99 \times 10^{+02}$
	8	$4.88 \times 10^{+01}$	$5.55 \times 10^{+01}$	$5.40 \times 10^{+01}$	$5.90 \times 10^{+01}$	$4.22 \times 10^{+01}$	$9.41 \times 10^{+01}$	$1.56 \times 10^{+02}$	$1.03 \times 10^{+02}$	$4.39 \times 10^{+02}$
	10	$5.79 \times 10^{+01}$	$6.01 \times 10^{+01}$	$6.43 \times 10^{+01}$	$7.31 \times 10^{+01}$	$5.35 \times 10^{+01}$	$1.16 \times 10^{+02}$	$1.72 \times 10^{+02}$	$1.17 \times 10^{+02}$	$5.62 \times 10^{+02}$
	2	4.30×10^{-03}	7.35×10^{-03}	1.84×10^{-02}	6.04×10^{-04}	2.33×10^{-04}	1.95×10^{-04}	3.76×10^{-01}	1.20×10^{-01}	4.61×10^{-01}
	4	2.18×10^{-02}	5.11×10^{-02}	4.51×10^{-02}	1.08×10^{-02}	5.60×10^{-03}	1.43×10^{-02}	6.31×10^{-01}	2.54×10^{-01}	$1.12 \times 10^{+00}$
10^{10}	6	1.05×10^{-01}	1.91×10^{-01}	1.49×10^{-01}	8.89×10^{-02}	5.61×10^{-02}	1.04×10^{-01}	$1.36 \times 10^{+00}$	7.52×10^{-01}	$3.56 \times 10^{+00}$
	8	3.21×10^{-01}	4.63×10^{-01}	4.06×10^{-01}	4.48×10^{-01}	3.26×10^{-01}	3.96×10^{-01}	$2.76 \times 10^{+00}$	$1.69 \times 10^{+00}$	$9.16 \times 10^{+00}$
	10	7.05×10^{-01}	8.89×10^{-01}	8.55×10^{-01}	$1.33 \times 10^{+00}$	$1.05 \times 10^{+00}$	$1.13 \times 10^{+00}$	$4.72 \times 10^{+00}$	$2.98 \times 10^{+00}$	$1.78 \times 10^{+01}$

| | | ^{118}Zr | | | ^{120}Zr | | |
$\rho\, Y_e$	T_9	$\lambda^{\mathrm{pn-QRPA-FRDM}}_{(\mathrm{EE+PC})}$	$\lambda^{\mathrm{pn-QRPA-DDPC1}}_{(\mathrm{EE+PC})}$	$\lambda^{\mathrm{pn-QRPA-DDME2}}_{(\mathrm{EE+PC})}$	$\lambda^{\mathrm{pn-QRPA-FRDM}}_{(\mathrm{EE+PC})}$	$\lambda^{\mathrm{pn-QRPA-DDPC1}}_{(\mathrm{EE+PC})}$	$\lambda^{\mathrm{pn-QRPA-DDME2}}_{(\mathrm{EE+PC})}$
	2	$1.52 \times 10^{+02}$	$2.38 \times 10^{+02}$	$2.38 \times 10^{+02}$	$2.91 \times 10^{+02}$	$2.91 \times 10^{+02}$	$2.91 \times 10^{+02}$
	4	$1.53 \times 10^{+02}$	$2.49 \times 10^{+02}$	$2.50 \times 10^{+02}$	$2.95 \times 10^{+02}$	$2.95 \times 10^{+02}$	$2.95 \times 10^{+02}$
10^4	6	$1.65 \times 10^{+02}$	$3.24 \times 10^{+02}$	$3.30 \times 10^{+02}$	$3.38 \times 10^{+02}$	$3.38 \times 10^{+02}$	$3.42 \times 10^{+02}$
	8	$1.94 \times 10^{+02}$	$4.65 \times 10^{+02}$	$4.88 \times 10^{+02}$	$4.55 \times 10^{+02}$	$4.56 \times 10^{+02}$	$4.77 \times 10^{+02}$
	10	$2.24 \times 10^{+02}$	$6.17 \times 10^{+02}$	$6.65 \times 10^{+02}$	$6.19 \times 10^{+02}$	$6.22 \times 10^{+02}$	$6.71 \times 10^{+02}$
	2	$1.50 \times 10^{+02}$	$2.36 \times 10^{+02}$	$2.36 \times 10^{+02}$	$2.88 \times 10^{+02}$	$2.88 \times 10^{+02}$	$2.88 \times 10^{+02}$
	4	$1.51 \times 10^{+02}$	$2.47 \times 10^{+02}$	$2.47 \times 10^{+02}$	$2.92 \times 10^{+02}$	$2.92 \times 10^{+02}$	$2.92 \times 10^{+02}$

Table 2
(Continued)

ρY_e	T_9	^{118}Zr			^{120}Zr		
		$\lambda_{(EE+PC)}^{pn-QRPA-FRDM}$	$\lambda_{(EE+PC)}^{pn-QRPA-DDPC1}$	$\lambda_{(EE+PC)}^{pn-QRPA-DDME2}$	$\lambda_{(EE+PC)}^{pn-QRPA-FRDM}$	$\lambda_{(EE+PC)}^{pn-QRPA-DDPC1}$	$\lambda_{(EE+PC)}^{pn-QRPA-DDME2}$
10^7	6	$1.64 \times 10^{+02}$	$3.22 \times 10^{+02}$	$3.27 \times 10^{+02}$	$3.36 \times 10^{+02}$	$3.36 \times 10^{+02}$	$3.41 \times 10^{+02}$
	8	$1.92 \times 10^{+02}$	$4.62 \times 10^{+02}$	$4.85 \times 10^{+02}$	$4.53 \times 10^{+02}$	$4.55 \times 10^{+02}$	$4.75 \times 10^{+02}$
	10	$2.23 \times 10^{+02}$	$6.14 \times 10^{+02}$	$6.62 \times 10^{+02}$	$6.17 \times 10^{+02}$	$6.20 \times 10^{+02}$	$6.69 \times 10^{+02}$
	2	$1.31 \times 10^{+00}$	$2.77 \times 10^{+00}$	$2.77 \times 10^{+00}$	$7.31 \times 10^{+00}$	$7.31 \times 10^{+00}$	$7.31 \times 10^{+00}$
	4	$1.74 \times 10^{+00}$	$3.86 \times 10^{+00}$	$3.87 \times 10^{+00}$	$8.69 \times 10^{+00}$	$8.69 \times 10^{+00}$	$8.71 \times 10^{+00}$
10^{10}	6	$2.82 \times 10^{+00}$	$7.29 \times 10^{+00}$	$7.43 \times 10^{+00}$	$1.26 \times 10^{+01}$	$1.26 \times 10^{+01}$	$1.29 \times 10^{+01}$
	8	$5.06 \times 10^{+00}$	$1.52 \times 10^{+01}$	$1.60 \times 10^{+01}$	$2.24 \times 10^{+01}$	$2.25 \times 10^{+01}$	$2.38 \times 10^{+01}$
	10	$8.41 \times 10^{+00}$	$2.80 \times 10^{+01}$	$2.99 \times 10^{+01}$	$3.96 \times 10^{+01}$	$3.99 \times 10^{+01}$	$4.35 \times 10^{+01}$
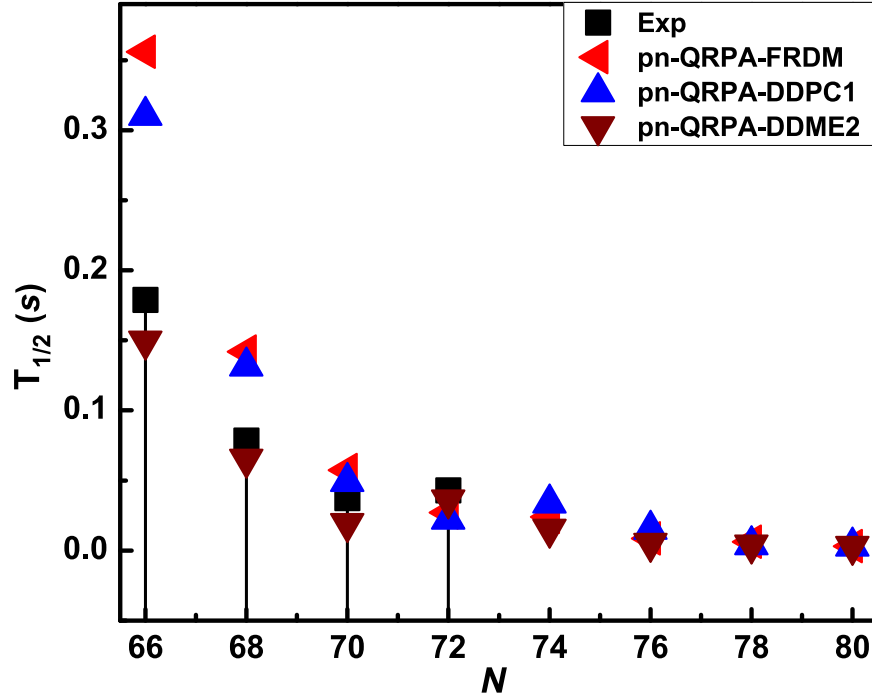
Figure 8. Comparison of the pn-QRPA-FRDM, pn-QRPA-DDPC1 and pn-QRPA-DDME2 calculated β-decay half-lives for Zr isotopes with experimental data (Wang et al. 2021).

4. Conclusion

The key findings and conclusions are outlined as follows: In the present work, we have analyzed the nuclear ground state and beta decay properties using the RMF and pn-QRPA models for the list of Zr isotopes with even mass nuclei ($A = 106$–120). The nuclear ground state properties including the PECs, β_2, S_n, S_{2n}, and r_{np} are analyzed. The RMF-based calculations were performed using the DDPC1 and DDME2 interactions. The RMF-based predictions show oblate shapes for $^{106-116}$Zr and spherical shapes for $^{118-120}$Zr using the DDPC1 interaction. Similarly, by employing the ME2 interaction, oblate shapes are predicted for $^{106-108}$Zr and spherical shapes are predicted for the remaining isotopes. Furthermore, we have analyzed the S_n, S_{2n}, and r_{np} for the same list of Zr nuclei. The present analysis is in decent agreement with measured data and previous predictions.

(1) The β_2 values computed via the RMF model were later used as input parameters in the pn-QRPA model to perform self-consistent calculations of the β-decay properties of Zr isotopes in the mass region $106 \leqslant A \leqslant 120$. The calculated GT distributions and half-lives were found to be in reasonable agreement with the measured data.

(2) The stellar weak interaction rates for Zr isotopes were computed in a fully microscopic fashion, without assuming the Brink-Axel hypothesis in the analysis of excited state GT distributions. The pn-QRPA-DDME2 rates are found to be higher than those of pn-QRPA-DDPC1 and pn-QRPA-FRDM. The reported weak rates computed using the pn-QRPA-DDME2 model are larger than those computed with pn-QRPA-DDPC1 and pn-QRPA-FRDM by as much as a factor of 1.3. Only at high temperature ($T_9 \geqslant 2$) and low density ($\rho Y_e \leqslant 10^7 \, \mathrm{g \, cm^{-3}}$) values, the sum of EE and PC rates has a sizeable contribution, with positive exponents, to the total stellar rates. The predicted stellar rates could prove useful for r-process nucleosynthesis calculations and future simulations of late-time stellar evolution.

Declaration of Competing Interest

The authors declare that they have no known competing financial interests or personal relationships that could have appeared to influence the work reported in this paper.

References

Bender, M., Bertsch, G. F., & Heenen, P.-H. 2008, PhRvC, 78, 054312
Burbidge, E. M., Burbidge, G. M., Fowler, W. A., & Hoyle, F. 1957, RvMP, 29, 547
Cowan, J. J., Thielemann, F.-K., & Truran, J. W. 1991, PhR, 208, 267
Fuller, G. M., Fowler, W. A., & Newman, M. J. 1982, ApJ, 252, 715
Gove, N. B., & Martin, M. J. 1971, ADNDT, 10, 205
Ha, J., Sumikama, T., Browne, F., et al. 2020, PhRvC, 101, 044311
Hardy, J. C., & Towner, I. C. 2009, PhRvC, 79, 055502
Hirsch, M., Staudt, A., Muto, K., & Klapdor-Kleingrothaus, H. V. 1991, NuPhA, 535, 62
Hirsch, M., Staudt, A., Muto, K., & Klapdor-Kleingrothaus, H. V. 1993, ADNDT, 53, 165
Homma, H., Bender, E., Hirsch, M., et al. 1996, PhRvC, 54, 2972
Ikeda, K., Fujii, S., & Fujita, J. I. 1963, PhL, 3, 271
Karatzikos, S., Afanasjev, A. V., Lalazissis, G. A., & Ring, P. 2010, PhLB, 689, 72
Klapdor, H. V., Metzinger, J., & Oda, T. 1984, ADNDT, 31, 81
Kumar, B., Singh, S. K., & Patra, S. K. 2014, IJMPE, 24, 1550017
Kabir, A., Nabi, J.-U., Tahir, M., Muneem, A., & Abideen, Z.U. 2024, ChPhC, 48, 094101
Lalazissis, G. A., Nikšić, T., Vretenar, D., & Ring, P. 2005, PhRvC, 71, 024312
Liu, Z. X., Lam, Y. H., Lu, N., & Ring, P. 2024, ADNDT, 156, 101635
McLaughlin, G. C., & Fuller, G. 1997, ApJ, 489, 766
Meng, J., Toki, H., Zhou, S., et al. 2006, PrPNP, 57, 470
Möller, P., Sierk, A. J., Ichikawa, T., & Sagawa, H. 2016, ADNDT, 109, 204
Muto, K., Bender, E., Oda, T., & Klapdor-Kleingrothaus, H. V. 1992, ZPhyA, 341, 407
Nabi, J. U., Bayram, T., Riaz, M., et al. 2023, PhS, 98, 085314
Nabi, J. U., Kabir, A., Khalid, W., Rida, S. A., & Anwaar, I. 2024, ChJPh, 92, 22
Nabi, J. U., & Klapdor-Kleingrothaus, H. V. 1999, ADNDT, 71, 149
Nabi, J. U., Ullah, A., Shah, S. A. A., Daraz, G., & Ahmad, M. 2019, AcPPB, 50, 1523
Nakamura, K. & Particle Data Group 2010, JPhG, 37, 075021
Ni, D., & Ren, Z. 2014, PhRvC, 89, 064320
Nikšić, T., Paar, N., Vretenar, D., & Ring, P. 2008, PhRvC, 78, 034318
Nikšić, T., Paar, N., Vretenar, D., & Ring, P. 2014, CoPhC, 185, 1808
Nilsson, S. G. 1955, Dan. Mat. Fys. Medd., 29, 16
Nomura, K., Rodriguez-Guzman, R., & Robledo, L. M. 2016, PhRvC, 94, 044314
Pereira, J., Hennrich, S., Aprahamian, A., et al. 2009, PhRvC, 79, 035806
Ring, P. 1996, PrPNP, 37, 193
Ragnarsson, I., & Sheline, R. K. 1984, PhyS, 29, 385
Sarriguren, P., Moya de Guerra, E., Pacearescu, L., & Faessler, A. 2003, PhRvC, 67, 044313
Sarriguren, P., & Pereira, J. 2010, PhRvC, 81, 064314
Skalski, J., Mizutori, S., & Nazarewicz, W. 1997, NuPhA, 617, 282
Staudt, A., Bender, E., Muto, K., & Klapdor-Kleingrothaus, H. V. 1999, ADNDT, 44, 79
Sumikama, T., Yoshinaga, K., Watanabe, H., et al. 2011, PhRvL, 106, 202501
Usman, S., & Mushtaq, A. 2023, NatSR, 13, 15315
Walecka, J. D. 1974, AnPhy, 83, 491
Wang, M., Huang, W. J., Kondev, F. G., Audi, G., & Naimi, S. 2021, ChPhC, 45, 030003
Wood, J. L., Heyde, K., Nazarewicz, W., Huyse, M., & Van Duppen, P. 1992, PhR, 215, 101
Xiang, J., Li, Z. P., Li, Z. X., Yao, J. M., & Meng, J. 2012, NuPhA, 873, 1
Yoshida, K., Niu, Y., & Minato, F. 2023, PhRvC, 108, 034305